



# Numerical analysis on dynamic behavior of solid oxide fuel cell with power output control scheme

Y. Komatsu <sup>a,\*</sup>, S. Kimijima <sup>b</sup>, J.S. Szmyd <sup>c</sup>

<sup>a</sup> Division of Regional Environment Systems, Graduated School of Engineering, Shibaura Institute of Technology, 307 Fukasaku, Minuma-ku, Saitama-shi, 337-8570 Saitama, Japan

<sup>b</sup> Department of Machinery and Control Systems, College of Systems Engineering and Science, Shibaura Institute of Technology, 307 Fukasaku, Minuma-ku, Saitama-shi, 337-8570 Saitama, Japan

<sup>c</sup> Department of Fundamental Research in Energy Engineering, Faculty of Energy and Fuels, AGH University of Science and Technology, 30 Mickiewicza Avenue, 30-059 Krakow, Poland

## H I G H L I G H T S

- Dynamic modeling of a solid oxide fuel cell (SOFC).
- Simulation of load-following operation with a multivariable control of SOFC.
- Cell operating temperature, fuel utilization factor and steam-to-carbon ratio controls.
- The cathode outlet temperature control for cell operating temperature maintenance.
- Discussion for responsiveness and fluctuation of response by controller specification.

## A R T I C L E I N F O

### Article history:

Received 4 July 2012

Received in revised form

28 August 2012

Accepted 14 September 2012

Available online 23 September 2012

### Keywords:

Solid oxide fuel cell

Dynamic modeling

Multivariable control scheme

Load-following operation

## A B S T R A C T

The present paper discusses the dynamic behavior of a solid oxide fuel cell (SOFC) system under the load-following operation with adoption of four control schemes, conducting dynamic simulation. The dynamic modeling of the SOFC, which consists of a cell stack and reformer, was firstly carried out to predict the dynamic behavior to load change. Secondly, a control circuit model was implemented into the dynamic model. For the load-following operation, the SOFC DC power output, operating temperature, fuel utilization factor and steam-to-carbon ratio were employed as the controlled variables. The current density, air, fuel and steam flow rates were chosen for manipulated variables in the SOFC control schemes for the load-following operation. Feedback control methodology was adopted to achieve adequate operation of the SOFC. The dynamic simulation was conducted by assuming the rapid change of the power. The simulation results showed the capability of the multivariable control of the SOFC operation. The cell temperature control is quite important, however the direct measure of the cell temperature is difficult. In the proposed control scheme, the air temperature at the cathode outlet is employed as a controlled variable, and then the cell temperature can be indirectly adjusted with controlling the cathode outlet temperature.

© 2012 Elsevier B.V. All rights reserved.

## 1. Introduction

High operating temperature solid oxide fuel cells (SOFCs) promise effective energy use, since they have potential to achieve higher energy conversion efficiency than conventional power generation systems. Hybrid power generation, which is integrated with a gas turbine, and combined heat and power application will contribute toward reducing primary energy consumption. Their

fuel flexibility promotes the use of SOFCs, and they may be suitable for distributed power generation. One of the bottlenecks of SOFCs for their commercialization is generally recognized as long term durability [1]. Therefore, the major attempt on SOFC development is aimed to achieve longer lifetime and high electrochemical performance in the material engineering field. Additionally, development of intermediate operating temperature type SOFCs is an important issue [2].

The design based on thermal management is another important subject on the SOFCs development. The high operating temperature causes the local hot spots and temperature gradient on the cell stack during the operation. The local hot spots and temperature

\* Corresponding author. Tel.: +81 48 687 5174; fax: +81 48 687 5197.

E-mail address: [m610101@sic.shibaura-it.ac.jp](mailto:m610101@sic.shibaura-it.ac.jp) (Y. Komatsu).

gradient can destroy the SOFC structure physically, hence the thermal management is important to mitigate thermal stress. In this context, the numerical modeling of the SOFC is recently recognized as useful tool. However, the proper thermal management requires the detailed modeling, which includes the considerable phenomena happening in the power generation process [3]. Li and Suzuki had presented detailed modeling of a tubular cell for pure hydrogen fuel case. They suggested that the air flow rate is a significant factor. The cell cooling effect by the air flow can contribute preventing a occurrence of the local hot spot on the cell [3]. Nishino et al. had also shown the detailed modeling of a tubular SOFC with an indirect internal reforming for methane fueled case [4]. It was noted that the thermal non-uniformity on the cell was leveled by increasing air flow rate however the excess air supply deteriorates the cell performance [4]. Moreover, Selimovic et al. had carried out the numerical analysis of the thermal stress on a planar type SOFC [5]. The investigation with the numerical modeling approach, becomes larger research activity. It will help to design durable cell geometry and to improve system package. A number of numerical investigations focus on steady-state modeling. Brus and Szmyd described a three-dimensional numerical model of heat transfer process in the module chamber of an internal indirect reforming-type SOFC [6].

Biomass is of particular interest as a viable energy source. Thus attempts have been made to use biogas produced from the anaerobic digestion of biomass as a fuel for high-temperature fuel cell systems such as SOFC [7]. A numerical study was performed by Nishino and Szmyd on the thermal and electrochemical characteristics of a tubular solid oxide fuel cell (SOFC) employing the steam reforming of biogas in each individual cell unit but indirectly from the anode [8]. Brus et al. has been numerically and experimentally investigated the process of reforming biogas on a Ni/YSZ and a Ni/SDC catalyst [7]. A numerical study on the performance of an SOFC-MGT hybrid system using biogas has been carried out by Komatsu et al. [9]. These results are, at least from the performance and thermal management point of view, quite promising for the future use of biogas fuels for the high-temperature, indirect internal reforming SOFC systems.

As one of majorly interests for the development of the SOFC system, hybrid system with gas turbine system was focused on those works [10–13]. Uechi et al. presented exergy analysis of hybridized SOFC system with gas turbine for a smaller scale generation system [11]. Stiller et al. carried numerical modeling for the hybrid system with both of a planar type and tubular type SOFC cells [10]. Those works propagated the attractiveness of the hybrid system. Among them, the importance of operation method was also discussed under part-load condition [12–14]. Those numerical investigations showed the estimation for performance analysis under full-load and part-load condition. They also suggest a conceptual operation tactic with the flexible gas turbine rotational speed operation to minimize SOFC's cell operating temperature variation under the part-load condition, which can accompanies to achieve highly efficient power generation performance [12,13]. Effort to control the operating temperature is an important attempt not only in terms of the safe operation but also the efficient operation.

Toward application to distributed energy system, the SOFC may be required to be operated flexibly in order to meet the power demand change. Understanding the transient characteristics is crucial issues in developing a control scheme of load-following. That will dedicate to create highly efficient operation methodology and to optimize the system design and packaging.

Bhattacharyya et al. showed the effect of mass diffusion on transient response of a cell performance with the dynamic modeling of a tubular SOFC and the simulation results were

validated by the comparison with the experimental results [15]. Gemmen and Johnson showed transient capability of a planar type SOFC with the dynamic modeling based on their assessment of the time scales of the physical and chemical phenomena [16]. At the same time, a number of papers have investigated the load-following performance of SOFC systems with dynamic system analysis [17–19]. In those work, the SOFC power output was controlled by manipulating the electric current in order to meet the power demand.

In the present paper, dynamic behavior of the SOFC is investigated in order to develop a control scheme. Dynamic simulation on the power output control of the SOFC with DC electric current adjustment was carried out in a previous paper [20]. In that simulation, air, fuel and steam inputs were kept constant to define the SOFC transient behavior without any control (except power output) and to evaluate load-following performance [20]. The power output responded quickly to the load changes, because the slow response of the cell temperature allowed for easy regulation of the electric current to eliminate the error in the power output. However, the cell performance under the part-load condition was degraded by the cell temperature drop due to the load decrease. A control tactic to optimize cell operating temperature is required for preventing deterioration of the cell voltage.

Under the part-load condition, the control of fuel utilization is also very important for improving efficiency. The adoption of the steam-to-carbon ratio ( $S/C$ ) control is indispensable for avoiding carbon deposition. During the load-following operation, the additional control schemes are required to optimize the operation to achieve the high system efficiency. The present paper describes the numerical simulation of the multivariable control scheme for SOFC operation with a power output control.

## 2. Numerical modeling

### 2.1. Model configuration

The configuration of the present SOFC module is shown in Fig. 1. The adopted SOFC system model was previously developed by Song et al. [21]. The numerical model was drawn up for steady-state performance analysis of an SOFC-micro gas turbine hybrid system [21]. In this study, the SOFC part was extracted and adopted for the dynamic simulation.

The SOFC module consists of the cell stack and the indirect internal reformer as shown in Fig. 1. Inside the cathode channel of the tubular cell, air is supplied through the air feed tube and flows from the bottom to the top of the cell. Fuel is supplied to the channel, which is configured by the fuel feed plates, and flows into the reforming channel separated by the reformer wall and the fuel feed plate. The reformed fuel is fed into the cell stack, and then the fuel participates in the electrochemical reaction.

For purposes of simplification, the cell stack is assumed to be single cell with the additional assumption. The air and fuel mass flow rates are equivalent in all cases and the thermal distribution in the  $y$ – $z$  cross section is small enough to be neglected. Consequently, the numerical model is one dimensional in the cell's longitudinal direction. The SOFC module is sliced into  $i$  segments, and the mass balance, the electrochemical reaction and heat balance are calculated in the each segment. Fig. 2 shows the heat transfer model in the present configuration. The heat conductions in the cell and the reformer wall, heat convection between solid parts and the working fluids and heat radiation occurring between the cell and the reformer are taken into the calculations.

In order to build the dynamic model as a useful prediction tool, the simple model is required for short computing time. However, the model must include significant factors on the dynamic

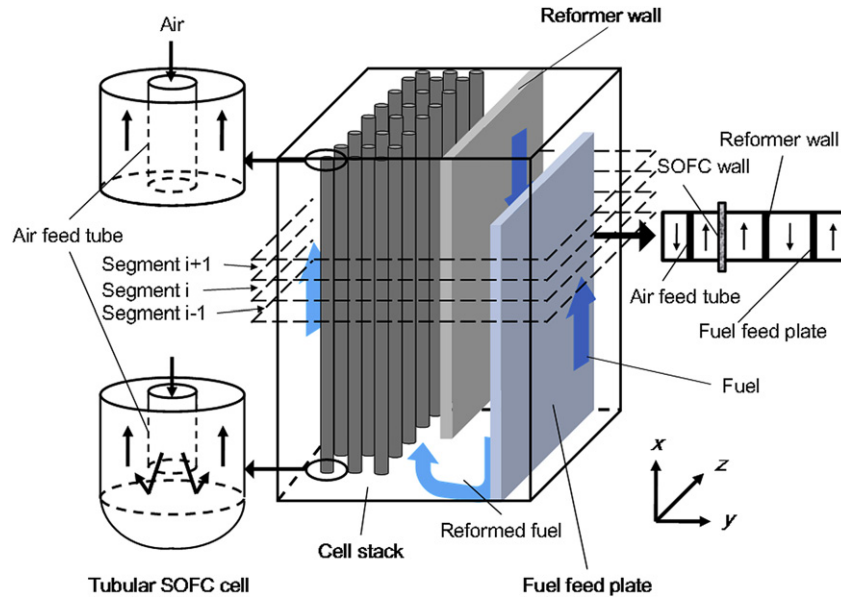


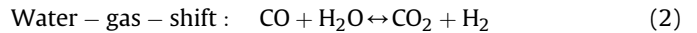
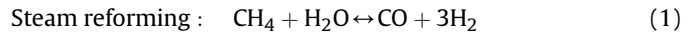
Fig. 1. Configuration of SOFC module.

characteristics of the SOFC. It is quite important to extract the prevailing phenomena from the dynamic behavior of the SOFC. Gemmen and Johnson have shown the time scales of all the physical and chemical phenomena in an SOFC [16]. The time scales span a wide range of time order. The present study focused on building a model which considered the significant phenomena governing the transient response, and then the developed dynamic model is composed of the steady mass balance and unsteady energy balance.

## 2.2. Chemical and electrochemical reactions

The SOFC power generation module (Fig. 1) adopts an indirect internal reforming type SOFC developed by Siemens Power Co., Ltd. [22]. The module consists of the internal reformer and cell stacks, which are bundles of a cathode-supported tubular type SOFC. The supplied fuel is reformed in the internal reformer with steam. In the

present work, fuel compositions are pure methane ( $\text{CH}_4$ ) and it is therefore assumed that the reforming process is dominated by the steam reforming reaction and water-gas-shift reaction as follows:



The steam reforming reaction is highly endothermic and reacts slowly, while the water–gas–shift reaction is a fast-reacting, weak exothermic one. The steam reforming reaction therefore strongly dominates the entire reforming process. The steam reforming reaction rate is sensitive to the temperature, the partial pressure of  $\text{CH}_4$  and catalysts [23]. The reaction rate of the steam reforming is determined using this formula [24]:

$$\dot{r}_{\text{CH}_4} = k_{\text{CH}_4} \exp\left(\frac{-E_{\text{CH}_4}}{RT}\right) p_{\text{CH}_4} \quad (3)$$

where  $k_{\text{CH}_4}$  ( $=4274 [\text{mol m}^{-2} \text{bar}^{-1} \text{s}^{-1}]$ ) is the pre-exponential factor,  $p_{\text{CH}_4}$  is the partial pressure of  $\text{CH}_4$  and  $E_{\text{CH}_4}$  ( $=82 [\text{kJ mol}^{-1}]$ ) is the activation energy of the steam reforming reaction [24]. In addition  $R$  stands for the gas constant, and  $T$  indicates the reaction temperature. Since the water–gas–shift reaction is fast, it can spontaneously reach equilibrium. The water–gas–shift reaction is therefore governed by the equilibrium constant determined in Eq. (4), but not by the reaction rate.

$$K_{\text{shift}} = \frac{p_{\text{CO}_2} \cdot p_{\text{H}_2}}{p_{\text{CO}} \cdot p_{\text{H}_2\text{O}}} \quad (4)$$

Since the chemical components in the working fluid flow are assumed to be ideal gases the equilibrium constant can be described as a function of the components' partial pressure. In the SOFC, both the  $\text{H}_2$  and  $\text{CO}$  generated through the reforming process can participate in the electrochemical reaction process [25].

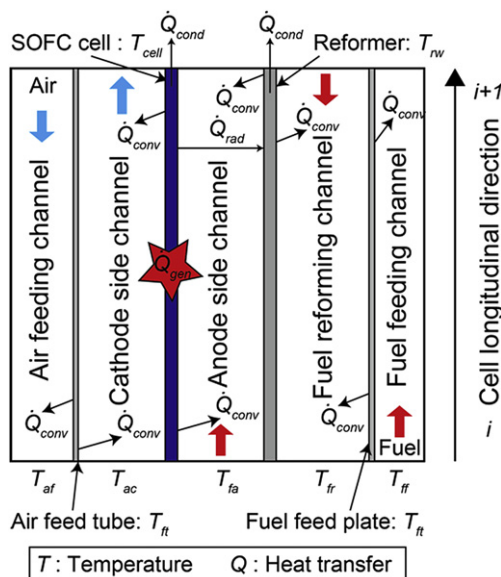
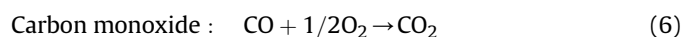
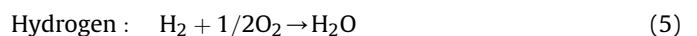


Fig. 2. Heat transfer model.

### 2.3. System performance

The electrical power produced by a fuel cell is the product of electric potential, i.e. voltage, and electric current. Maximum available power  $\dot{W}_{\text{SOFC,max}}$  produced by the electrochemical reaction in a fuel cell is equal to the difference in the Gibbs free energy  $\Delta\bar{G}$  between products and reactants of the electrochemical reaction, which can be expressed by a function of open circuit voltage (OCV),  $V_{\text{OC}}$  (i.e. the Nernst potential) [21]:

$$\dot{W}_{\text{SOFC,max}} = -\Delta\dot{G} = -(z_{\text{H}_2} + z_{\text{CO}})\Delta\bar{g} = 2(z_{\text{H}_2} + z_{\text{CO}})FV_{\text{OC}} \quad (7)$$

where  $z$  indicates the amount of consumed fuel in mol  $[\text{kmol s}^{-1}]$ . Since the chemical compositions are treated as an ideal gas, the change in the Gibbs free energy per 1 mol of  $\text{H}_2$  can be expressed as:

$$-\Delta\bar{g} = -\Delta\bar{g}^0 + RT \ln \left[ \frac{p_{\text{H}_2}/p_0 \cdot (p_{\text{O}_2}/p_0)^{1/2}}{p_{\text{H}_2\text{O}}/p_0} \right] \quad (8)$$

The difference in the Gibbs free energy per 1 mol of carbon monoxide is equal to that of hydrogen because the shift reaction is assumed at equilibrium [24]. It means that open circuit voltages of hydrogen and carbon monoxide are same. Thermodynamic data of the open circuit voltage for  $\text{H}_2$  and  $\text{CO}$ , computed in the present model for simulation of the electrochemical reaction, is indicated in Table 1. By defining the current density  $j$  as the transfer rate of electron per unit active area of the fuel cell, the electric power produced by the fuel cell can be expressed as:

$$\dot{W}_{\text{SOFC}} = V_{\text{cell}}jA = [V_{\text{OC}} - (\Delta V_{\text{act}} + \Delta V_{\text{ohm}})]jA \quad (9)$$

where  $\Delta V_{\text{act}}$  is the activation polarization and  $\Delta V_{\text{ohm}}$  is the ohmic polarization. The concentration loss is neglected in the present study, since the transient characteristic of mass diffusion in porous electrodes are very fast phenomena in the transient characteristics which possess SOFC. The net cell voltage  $V_{\text{cell}}$  is the difference between the open circuit voltage and the voltage losses due to the phenomena that occurred in the electron transfer. The activation polarization and the ohmic losses are included in the estimation of the voltage loss and Achenbach's empirical equations are adopted for the activation polarization [24].

$$\Delta V_{\text{act}} = j r_c + j_{\text{H}_2} r_{\text{a,H}_2} = j r_c + j_{\text{CO}} r_{\text{a,CO}} \quad (10)$$

where

$$j = j_{\text{H}_2} + j_{\text{CO}} \quad (11)$$

with

$$\text{Cathode, Oxygen: } \frac{1}{r_c} = \frac{4F}{RT} k_c \left( \frac{p_{\text{O}_2}}{p_0} \right)^{0.25} \exp \left( -\frac{E_c}{RT} \right) \quad (12)$$

**Table 1**

Thermodynamic data of open circuit voltage (OCV) in electrochemical reaction conducted with present numerical model with equilibrium assumption for water–gas-shift reaction (anode inlet condition with  $\text{CH}_4 = 6.10 \times 10^{-2}$ ,  $\text{H}_2 = 1.51$ ,  $\text{CO} = 2.93 \times 10^{-1}$ ,  $\text{CO}_2 = 1.58 \times 10^{-1}$  and  $\text{H}_2\text{O} = 6.67 \times 10^{-1}$   $[\text{mol s}^{-1}]$  and cathode inlet condition with  $\text{O}_2 = 8.45$   $[\text{mol s}^{-1}]$ ) (the values are averaged in longitudinal direction of reaction path).

Temperature [K]	OCV for $\text{H}_2$ [V]	OCV for $\text{CO}$ [V]
1113	0.976	0.975
1137	0.967	0.967
1163	0.959	0.959
1200	0.948	0.948
1220	0.942	0.942

$$\text{Anode, Hydrogen: } \frac{1}{r_{\text{a,H}_2}} = \frac{2F}{RT} k_{\text{a,H}_2} \left( \frac{p_{\text{H}_2}}{p_0} \right)^{0.25} \exp \left( -\frac{E_a}{RT} \right) \quad (13)$$

$$\text{Anode, Carbon monoxide: } \frac{1}{r_{\text{a,CO}}} = \frac{2F}{RT} k_{\text{a,CO}} \left( \frac{p_{\text{CO}}}{p_0} \right)^{0.25} \exp \left( -\frac{E_a}{RT} \right) \quad (14)$$

where,  $r$  means that the area specific electrical resistance  $[\Omega \text{ m}^2]$ . Activation energies of the cathode and anode are set at  $E_c = 160$  and  $E_a = 110$   $[\text{kJ mol}^{-1}]$ . The pre-exponential factors are given at  $k_c = 1.491010$ ,  $k_{\text{a,H}_2} = 2.13108$  and  $k_{\text{a,CO}} = 2.98108$   $[\text{A m}^{-2}]$ . The ohmic losses in the tubular SOFC are considered not only for the radial ionic current across the electrolyte, but also for the circumferential electric current through the anode and cathode as indicated in Fig. 3 [21,26–28].

$$\Delta V_{\text{ohm}} = \Delta V_{\text{ohm,a}} + \Delta V_{\text{ohm,c}} + \Delta V_{\text{ohm,e}} + \Delta V_{\text{ohm,i}} \quad (15)$$

with

$$\text{Anode: } \Delta V_{\text{ohm,a}} = \frac{j \varepsilon_a (A \pi D_{\text{out}})^2}{8 d_a} \quad (16)$$

$$\text{Cathode: } \Delta V_{\text{ohm,c}} = \frac{j \varepsilon_c (\pi D_{\text{in}})^2}{8 d_c} A [A + 2(1 - A - B)] \quad (17)$$

$$\text{Electrolyte: } \Delta V_{\text{ohm,e}} = j \varepsilon_e d_e \quad (18)$$

$$\text{Interconnect: } \Delta V_{\text{ohm,int}} = j (\pi D_{\text{out}}) \varepsilon_{\text{int}} \frac{d_{\text{int}}}{w_{\text{int}}} \quad (19)$$

where  $A$  and  $B$  indicates the geometric parameter in Fig. 3 [21]. Adopted specific resistivity of the SOFC materials  $\varepsilon$   $[\Omega \text{ m}]$  are shown in the following equations [26].

$$\text{Anode: } \varepsilon_a = 2.98 \times 10^{-3} \exp \left( \frac{-1392}{T} \right) \quad (20)$$

$$\text{Cathode: } \varepsilon_c = 8.114 \times 10^{-3} \exp \left( \frac{-600}{T} \right) \quad (21)$$

$$\text{Electrolyte: } \varepsilon_e = 2.94 \times 10^{-3} \exp \left( \frac{-10350}{T} \right) \quad (22)$$

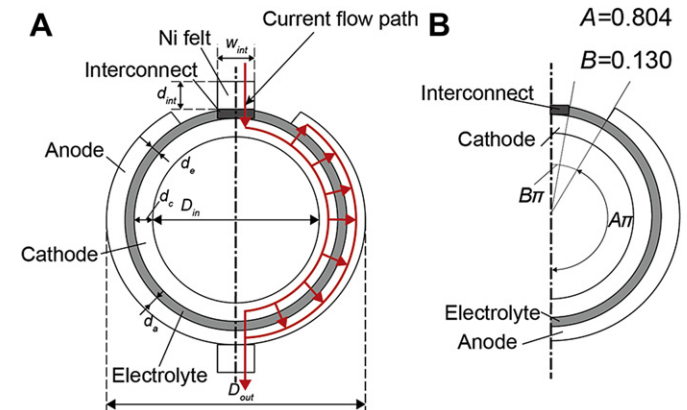


**Fig. 3.** A) Path of an electron/ion in tubular SOFC, B) half of a tubular SOFC.

$$\text{Interconnect : } \varepsilon_{\text{int}} = 1.256 \times 10^{-1} \exp\left(\frac{-1100}{T}\right) \quad (23)$$

where  $T$  is the temperature [K] for each of the cell components. The power generation efficiency of the SOFC  $\eta_{\text{SOFC}}$  is finally defined as:

$$\eta_{\text{SOFC}} = \frac{\dot{W}_{\text{SOFC}}}{\dot{m}_{\text{CH}_4} \times (\text{LHV})_{\text{CH}_4}} \quad (24)$$

The lower heating value (LHV) of  $\text{CH}_4$  is used.

#### 2.4. Dynamic modeling

Formulating unsteady energy equations, which are considered with heat transfer in the SOFC module, is indicated in the present section. Fig. 2 shows the heat transfer model in the SOFC module. The present dynamic modeling, the module is separated to three parts, i.e. air feeding channel side, fuel feeding channel side, and the SOFC cell stack parts.

##### 2.4.1. Air feeding channel

The governing unsteady energy equation for the air inside the air feed tube is described as follows:

$$\rho_{\text{af}} V_{\text{af}} c_{p,\text{af}} \frac{dT_{\text{af},i}}{dt} = \sum \dot{n}_{x,i} \bar{h}_x(T_{\text{af},i}) - \sum \dot{n}_{x,i+1} \bar{h}_x(T_{\text{af},i+1}) - h_{a1} A_{\text{ft}} (T_{\text{ft},i} - T_{\text{af},m}) \quad (25)$$

where  $h_{a1}$  is the heat transfer coefficient [ $\text{kW m}^{-2} \text{K}^{-1}$ ] between the air flow and the air feed tube. The unsteady energy equation of the air in the anode side channel can be described as:

$$\rho_{\text{ac}} V_{\text{ac}} c_{p,\text{ac}} \frac{dT_{\text{ac},i}}{dt} = \sum \dot{n}_{x,i} \bar{h}_x(T_{\text{ac},i}) - \sum \dot{n}_{x,i+1} \bar{h}_x(T_{\text{ac},i+1}) + h_{a2} A_{\text{cell}} (T_{\text{cell},i} - T_{\text{ac},m}) + h_{a3} A_{\text{ft}} \times (T_{\text{ft},i} - T_{\text{ac},m}) - \dot{Q}_{\text{elec,ox}} \quad (26)$$

with the heat efflux from the air to the cell due to oxygen diffusion:

$$\dot{Q}_{\text{elec,ox}} = \frac{1}{2} (z_{\text{H}_2} + z_{\text{CO}}) \bar{h}_{\text{O}_2} (T_{\text{ac},m}) \quad (27)$$

where  $h_{a2}$  is the heat transfer coefficient [ $\text{kW m}^{-2} \text{K}^{-1}$ ] between the air flow and the cell,  $h_{a3}$  is the heat transfer coefficient [ $\text{kW m}^{-2} \text{K}^{-1}$ ] between the air flow and the air feed tube wall. The unsteady energy equation for the air feed tube considered only the heat convection terms with the air flow in both side of the air feed tube can be described:

$$\rho_{\text{ft}} V_{\text{ft}} c_{\text{ft}} \frac{dT_{\text{ft},i}}{dt} = -h_{a1} A_{\text{ft}} (T_{\text{ft},i} - T_{\text{af},m}) - h_{a3} A_{\text{ft}} (T_{\text{ft},i} - T_{\text{ac},m}) \quad (28)$$

##### 2.4.2. Fuel feeding channel

The unsteady energy equation for the fuel flow in the channel, where is separated by the fuel feed plate, is described as follows:

$$\rho_{\text{ff}} V_{\text{ff}} c_{p,\text{ff}} \frac{dT_{\text{ff},i}}{dt} = \sum \dot{n}_{x,i} \bar{h}_x(T_{\text{ff},i}) - \sum \dot{n}_{x,i+1} \bar{h}_x(T_{\text{ff},i+1}) + h_{f1} A_{\text{fp}} (T_{\text{fp},i} - T_{\text{ff},m}) \quad (29)$$

where  $h_{f1}$  is the heat transfer coefficient [ $\text{kW m}^{-2} \text{K}^{-1}$ ] between the fuel flow and the fuel feed plate. The unsteady energy equation for the fuel in the reforming process can be described:

$$\rho_{\text{fr}} V_{\text{fr}} c_{p,\text{fr}} \frac{dT_{\text{fr},i}}{dt} = \sum \dot{n}_{x,i+1} \bar{h}_x(T_{\text{fr},i+1}) - \sum \dot{n}_{x,i} \bar{h}_x(T_{\text{fr},i}) + h_{r1} A_{\text{rw}} (T_{\text{rw},i} - T_{\text{fr},m}) + h_{r2} A_{\text{fp}} (T_{\text{fp},i} - T_{\text{fr},m}) \quad (30)$$

where  $h_{r1}$  is the heat transfer coefficient [ $\text{kW m}^{-2} \text{K}^{-1}$ ] between the fuel flow and the reformer wall,  $h_{r2}$  is the heat transfer coefficient [ $\text{kW m}^{-2} \text{K}^{-1}$ ] between the fuel flow and the fuel feed plate. The unsteady energy equation of the fuel feed plate considered with only heat convection terms can be described as:

$$\rho_{\text{fp}} V_{\text{fp}} c_{p,\text{fp}} \frac{dT_{\text{fp},i}}{dt} = -h_{r2} A_{\text{fp}} (T_{\text{fp},i} - T_{\text{fr},m}) - h_{f1} A_{\text{fp}} (T_{\text{fp},i} - T_{\text{ff},m}) \quad (31)$$

The unsteady energy equation for the reformer wall can be described as follows:

$$\rho_{\text{rw}} V_{\text{rw}} c_{p,\text{rw}} \frac{dT_{\text{rw},i}}{dt} = -h_{f2} A_{\text{rw}} (T_{\text{rw},i} - T_{\text{fr},m}) - h_{r1} A_{\text{rw}} \times (T_{\text{rw},i} - T_{\text{fr},m}) - \lambda_{\text{rw}} S_{\text{rw}} \Delta x \frac{d^2 T_{\text{rw},i}}{dx^2} + \dot{Q}_{\text{rad}} \quad (32)$$

with the radiative heat transfer occurring between the reformer wall and the SOFC:

$$\dot{Q}_{\text{rad}} = \sigma A_{\text{rw}} \sum_{j=1}^N \frac{(T_{\text{cell},i}^4 - T_{\text{rw},j}^4)}{\frac{1 - \varepsilon_{\text{cell}}}{\varepsilon_{\text{cell}}} + \frac{1}{F_{i-j}} + \frac{1 - \varepsilon_{\text{rw}}}{\varepsilon_{\text{rw}}}} \quad (33)$$

where  $\lambda_{\text{rw}}$  is the thermal conductivity [ $\text{kW m}^{-1} \text{K}^{-1}$ ] of the reformer wall and set at  $10 \times 10^{-3}$  [ $\text{kW m}^{-1} \text{K}^{-1}$ ].  $S$  is cross section area [ $\text{m}^2$ ],  $\sigma$  is the Stefan–Boltzmann constant,  $\varepsilon$  is emissivity (set at 0.85) and  $F$  is the configuration factor. Hottel's strings rule is employed to estimate the configuration factor [29]. The unsteady energy equation of the fuel flowing in the anode side channel is described as follows:

$$\rho_{\text{fa}} V_{\text{fa}} c_{p,\text{fa}} \frac{dT_{\text{fa},i}}{dt} = \sum \dot{n}_{x,i} \bar{h}_x(T_{\text{fa},i}) - \sum \dot{n}_{x,i+1} \bar{h}_x(T_{\text{fa},i+1}) + h_{f1} A_{\text{c}} (T_{\text{c},i} - T_{\text{fa},m}) + h_{f2} A_{\text{rw}} (T_{\text{rw},i} - T_{\text{fa},m}) - \dot{Q}_{\text{elec,fuel}} \quad (34)$$

with the heat efflux from the fuel to the cell due to the diffusion:

$$\dot{Q}_{\text{elec,fuel}} = z_{\text{H}_2} [\bar{h}_{\text{H}_2}(T_{\text{fa},m}) - \bar{h}_{\text{H}_2\text{O}}(T_{\text{cell},i})] + z_{\text{CO}} [\bar{h}_{\text{CO}}(T_{\text{fa},m}) - \bar{h}_{\text{CO}_2}(T_{\text{cell},i})] \quad (35)$$

##### 2.4.3. SOFC cell stack

The anode and cathode electrodes and the electrolyte are treated as the one component in the present model. Then the unsteady energy equation is given as:

$$\rho_{\text{cell}} V_{\text{cell}} c_{\text{cell}} \frac{dT_{\text{cell},i}}{dt} = -h_{a2} A_{\text{cell}} (T_{\text{cell},i} - T_{\text{ac},m}) - h_{f1} A_{\text{cell}} \times (T_{\text{cell},i} - T_{\text{fa},m}) - \lambda_{\text{cell}} S_{\text{cell}} \Delta x \frac{d^2 T_{\text{cell},i}}{dx^2} - \dot{W}_{\text{fc}} - \dot{Q}_{\text{rad}} + (\dot{Q}_{\text{elec,ox}} + \dot{Q}_{\text{elec,fuel}}) \quad (36)$$



where  $\dot{W}_{fc}$  is the done electric power [kW]. The thermal conductivity of the cell  $\lambda_{cell}$  is set at  $10 \times 10^{-3}$  [kW m<sup>-1</sup> K<sup>-1</sup>].

### 2.5. Control scheme of the SOFC operation

The present study focuses on building a control scheme for the load-following operation. Feedback control methodology is employed to control the DC power output, the cell operating temperature, the fuel utilization factor and S/C. Fig. 4 shows the multivariable control diagram for the SOFC operation.

In the each controller, the error  $e(t)$  is calculated as the difference between the reference value  $x(t)$  and the process value  $y(t)$ :

$$e(t) = x(t) - y(t). \quad (37)$$

P controller attempts to eliminate the error by adjusting manipulated variable  $MV(t)$ . In the case of proportional (P) control, the variation of the manipulated variable  $\Delta MV$  is described as follows:

$$\Delta MV = MV(t + \Delta t) - MV(t) = K_p e(t) \quad (38)$$

where  $K_p$  indicates the proportional gain. However, it is noted that the response time of the controller as indicated with  $\Delta t$ , depends on the time step of the dynamic simulation as indicated with  $dt$  in the unsteady energy balance equations.

The following are the correlations between the process variables and the manipulated variables in the present control schemes:

- For the purpose of the DC power output control, the current density is assumed to be as a manipulated value [17–20].
- The fuel utilization factor, which is calculated by the current density and the fuel molar flow rate as shown in Eq. (39), is controlled by manipulating the fuel mass flow rate [17,18].

$$U_f \equiv \frac{z_{H_2} + z_{CO}}{4\dot{n}_{CH_4, supplied}} = \frac{(I/2F)}{4\dot{n}_{CH_4, supplied}} = \frac{jA}{8F\dot{n}_{CH_4, supplied}} \quad (39)$$

- S/C, which is determined by the steam molar flow rate to the fuel molar flow rate in Eq. (40), is controlled by manipulating the steam mass flow rate corresponding to the fuel mass flow rate [17,18].

$$S/C = \frac{\dot{n}_{H_2O, supplied}}{\dot{n}_{CH_4, supplied}} \quad (40)$$

- Maintaining the cell temperature at the rated level by manipulating the air flow rate can ensure efficient operation and

**Table 2**  
System operating conditions.

System condition	Ambient temperature [K]	288
	Ambient pressure [atm]	1
Fuel cell condition	Net DC total power [kW] <sup>a</sup>	185
	Steam-to-carbon ratio	2.5
	Fuel utilization factor	0.85
	Average current density [A/m <sup>2</sup> ] <sup>a</sup>	3200
	Cell average temperature [K] <sup>a</sup>	1200
	Air inlet temperature [K]	1073
	Fuel inlet temperature [K]	873

<sup>a</sup> Parameter for design point analysis.

minimizing thermal stress and fatigue variation [17,18,30,31]. However, measuring the cell average temperature is substantially impossible. Hence, the air flow temperature at the cathode outlet is controlled at the appropriate temperature to control the cell average temperature indirectly by manipulating the air flow rate.

## 3. Results and discussion

### 3.1. Preliminary

The design point analysis was firstly carried out to determine the initial condition of the dynamic simulation. Table 2 shows the system operating condition of the design point analysis and dynamic simulation. For the design point analysis, the rated power output of the SOFC module is set at 185 [kW], where the average current density reached 3200 [A/m<sup>2</sup>] and the cell average temperature reached 1200 [K]. Table 3 shows the initial condition for the dynamic simulation. Table 4 shows the controller gains used for the each manipulated variable. Table 5 shows the thermophysical properties of the system components used for the dynamic simulation. The cell is treated as one composite, hence the thermophysical property of the cell is averaged by the weight of the electrodes, the electrolyte and the interconnect.

### 3.2. Simulation of dynamic behavior with multivariable control scheme

#### 3.2.1. Simulation setting and assumption

In order to evaluate the load-following performance, the power output is assumed to be decreased from 100% to 80% at 0.5 [min], and then assumed to be increased from 80% to 85% at 250 [min].

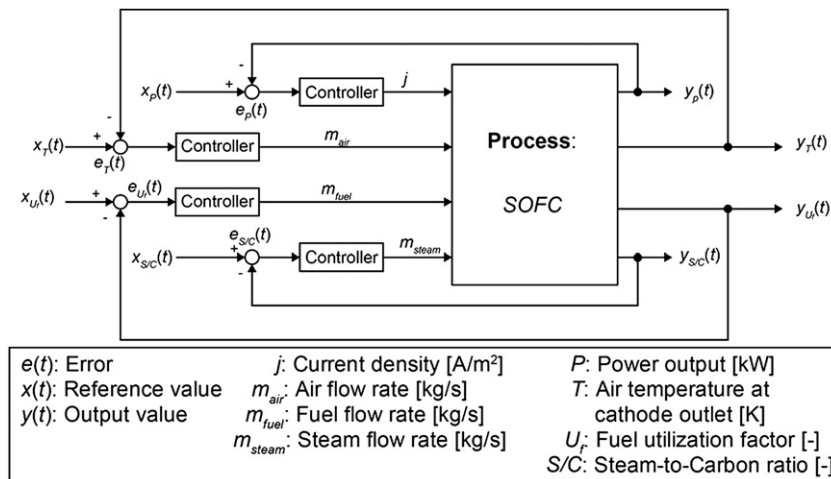


**Fig. 4.** Diagram of multivariable control scheme for SOFC operation.

**Table 3**

Initial dynamic simulation condition obtained by design point analysis.

Parameter	Value
Air mass flow rate [ $\text{kg s}^{-1}$ ]	1.176
Fuel mass flow rate [ $\times 10^{-3} \text{ kg s}^{-1}$ ]	8.2
Steam input [ $\times 10^{-2} \text{ kg s}^{-1}$ ]	2.3
Cell voltage [V]	0.55
Cell active area [ $\text{m}^2$ ]	105
Efficiency [%]	45.0

The step width of the time development simulation is set at 1 [s]. It means that the corrective actions are made by the controllers every second. During the load transient, the fuel flow rate and steam flow rate are manipulated to satisfy the reference fuel utilization factor of 0.85 and the reference S/C of 2.5. Though there is an actual delay due to mass transportation, it is assumed that all the manipulation is conducted quickly enough to neglect the time delay. However, the transient time of the temperature response could not be neglected so the saturation of the manipulated variable should be adopted for the control circuit [17]. Thus, the detailed control diagram of the cell operating temperature control scheme is redrawn in Fig. 5 with the power output control scheme.

### 3.2.2. Preliminary for air cathode outlet temperature control scheme

Fig. 6 shows the relationship between the required air flow rate and the power output under the operation for the constant cell average temperature at 1200 [K]. Decreasing the power output, the required air flow rate should be reduced in order to keep the cell average temperature at the rated value. The air flow temperature at the cathode outlet also decreases together with the decreasing power output, as shown in Fig. 7. The air flow rates of 1.176, 0.738 and 0.663 [ $\text{kg s}^{-1}$ ] are required for the power outputs of 100, 85 and 80%, respectively. The reference in the cell temperature management is the air temperature at the cathode outlet, and its value depends on the power output as indicated in Fig. 7. The reference value in the temperature control scheme is varied with the power output changing along the curve in Fig. 7. Its characteristic is also considered and implemented into the control diagram of the control schemes in Fig. 5.  $G$  expresses a function to set the reference value of the air cathode outlet temperature to the power output in Fig. 5.

### 3.2.3. Transient response of power output

Figs. 8 and 9 show the transient response of the power output under the load-following operation. The power output is well controlled, and then its response converged in 0.5 [min] in the case of decreasing the load from 100% to 80%. In the load increasing case, almost same behavior is appeared. However the, the steady-state errors still remain in all cases, since the proportional controller is adopted. These results show the effectiveness of the power output control with the current manipulation.

Fig. 10 shows the current density manipulation, and Fig. 11 the transient response of the cell voltage. In order to follow the rapid load changing, the controller manipulates the current density with

**Table 4**

Controller gains used for each P controller.

Variable	Controller gain
$K_p$ for current density	10 [ $\text{A m}^{-2} \text{ kW}^{-1}$ ]
$K_p$ for air flow rate	1 [ $\text{g s}^{-1} \text{ K}^{-1}$ ]
$K_p$ for fuel flow rate	-1 [ $\text{g s}^{-1}$ ]
$K_p$ for steam flow rate	1 [ $\text{g s}^{-1}$ ]

**Table 5**

Thermophysical properties of system components.

	Density [ $\text{kg m}^{-3}$ ]	Specific heat [kJ $\text{kg}^{-1} \text{ K}^{-1}$ ]
<i>SOFC</i>		
Anode: Ni/YSZ	7128	0.444
Cathode: LaMnO <sub>3</sub>	6600	0.432
Electrolyte: YSZ	5940	0.630
Interconnect: LaCrO <sub>3</sub>	6770	0.551
<i>Internal reformer</i>		
Ni/YSZ	7128	0.444
<i>Air feed tube, fuel feed plate</i>		
Stainless steel	7700	0.460

the large proportion according to the large deference between the reference and the actual processed value of the power output, and then the cell voltage varies considerably. The cell voltage changes with the cell temperature, since the electromotive force and the potentials depend on the cell temperature. However, as shown in following subsection, the transient response of the cell temperature is very slow comparing to the voltage change to the current manipulation. As a result, the power output can be controlled by manipulating the current without taking the effect of the cell temperature response on the cell voltage into consideration.

### 3.2.4. Fuel utilization factor and S/C controls

The fuel flow rate manipulation and the transient response of the fuel utilization factor are shown in Fig. 12. The steam flow rate manipulation and the transient response of the S/C are shown in Fig. 13. The flow rates become almost constant just after detecting the errors, and the processed variable immediately meets the reference values. The manipulated flow rates slightly fluctuate due to the current density manipulation. The fuel and steam flow rate manipulations, compared to the current manipulation, have the slower transient capability (order of second) and cause larger time-delay to the system due to the fuel processing and disturbance [32].

### 3.2.5. Cell temperature control

Fig. 14 shows the transient response of the cell average temperature, the air temperature at the cathode outlet and the reference temperature. Fig. 15 shows the air flow rate manipulation. Both the cell average temperature and the air cathode outlet temperature start to change with the load change. The air flow rate manipulation proceeded immediately before reaching the required temperatures in both cases of decreasing and increasing the power outputs. Consequently, the cell average temperature is kept at the rated level, though the response is slow after the load changes. This result means that the cell temperature can be controlled indirectly by the air temperature control at the cathode outlet. Figs. 16 and 17 show the temperature distributions of the SOFC under the increasing and decreasing power outputs, respectively. In the case of the large load decreasing, the temperature drop at the initial

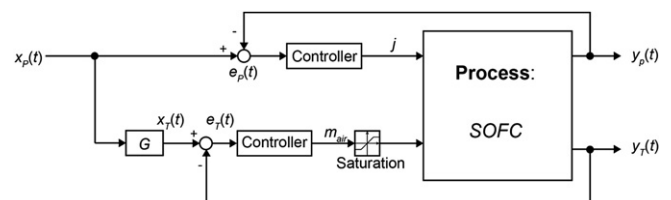


**Fig. 5.** Detailed control diagram of cell temperature control scheme with power output control.

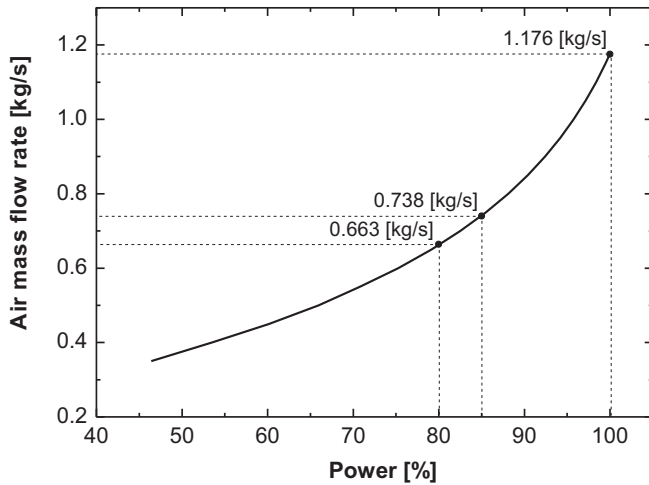


Fig. 6. Air flow rate under cell average temperature of 1200 [K].

response is very large, however the temperature distribution doesn't change fatally as shown in Fig. 16. The cell temperature at the outlet of air and fuel flow channel, i.e. the cell length of 1500 [mm], changes substantially. In the case of the small load change, the temperature distribution changes slightly as shown in Fig. 17. The control of the air temperature at the cathode outlet can prevent the fatal change on the cell temperature distribution. The appropriate reference settings of the air flow rate and the cathode outlet temperature are required for adopting the present control scheme in practical use.

### 3.3. Effect of multivariable control on power generation efficiency

Fig. 18 shows the DC efficiency of the SOFC power outputs under the full-load and the part-load conditions. The cell operating temperature of 1200 [K] and the fuel utilization of 85% are satisfied at the steady-state in all cases. The DC efficiency is 45.0% at the rated condition in the present simulation. The DC efficiencies at the part-load of 80% and 85% reach 52.8% and 51.2%, respectively. As clearly can be seen in Fig. 18, the much higher efficiency can be performed under the part-load condition of the smaller power output. Fig. 18 also shows the DC efficiencies affected by the fuel

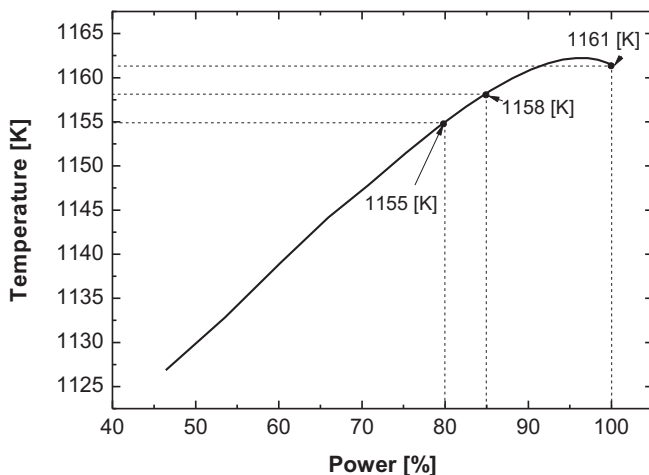


Fig. 7. Air temperature at cathode outlet under cell average temperature of 1200 [K].

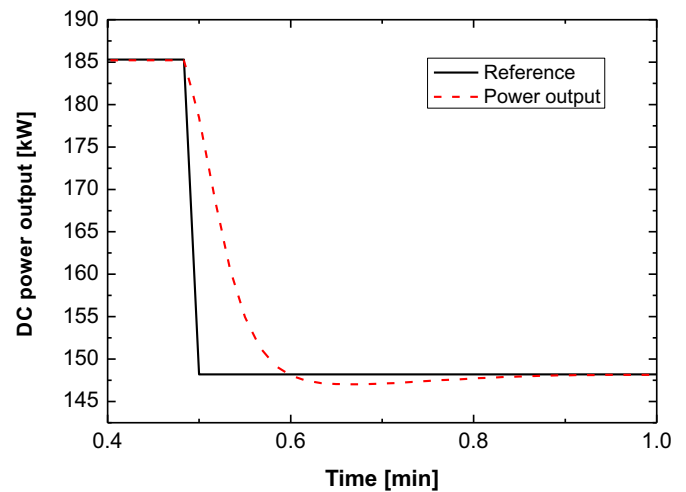


Fig. 8. Transient response of DC power output following simulated load change (power output from 100% to 80%).

utilization and the cell temperature control schemes during the operation, respectively. The comparison is also indicated at the operation result without any control, where any kind of the variables are not referred under the load-following operation. The DC efficiencies in the case without any control and with the cell temperature control have similar trend to the power output change. It is noted that the both operations don't have any functional control methodology for the fuel provision, and then the constant fuel is supplied in spite of the load changes. Fig. 19 shows the comparison of the cases with the cell temperature control and without any control (the cell temperature in Fig. 19A, the cell voltage in Fig. 19B, Performed current density in Fig. 19C and the fuel utilization in Fig. 19D under both of the case with cell temperature control and the case without any control). The cell temperature with the cell temperature control is higher than the one without any control, hence the current with the cell temperature control is smaller than the one without any control as shown in Fig. 19. The cell voltage is kept high in the case with the cell temperature control. It is not necessary to operate the current density at high in order to perform the required power output

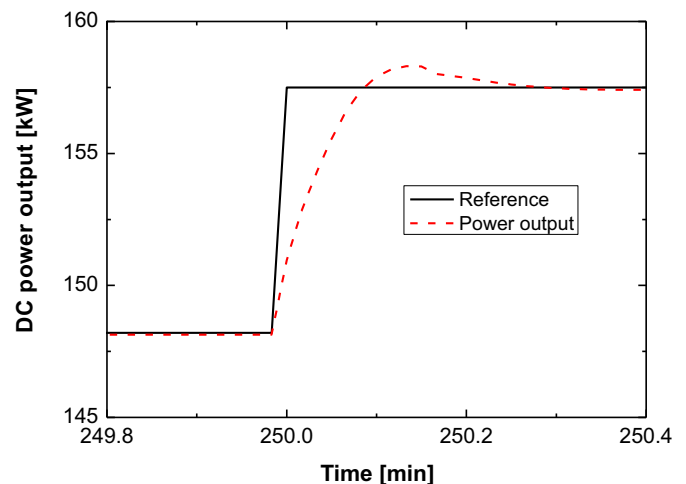


Fig. 9. Transient response of DC power output following simulated load change (power output: from 80% to 85%).



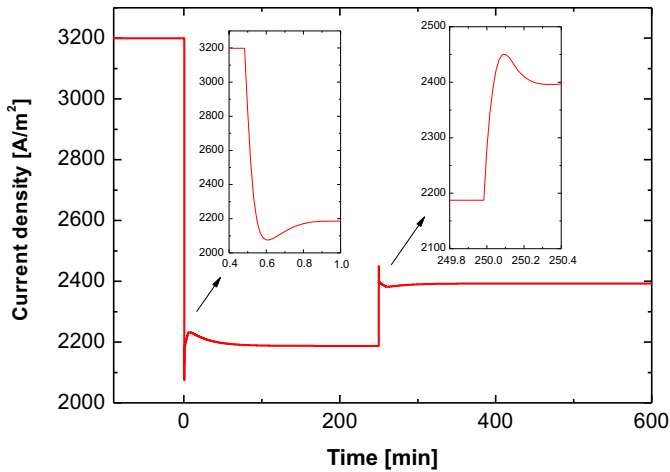


Fig. 10. Current density manipulation.

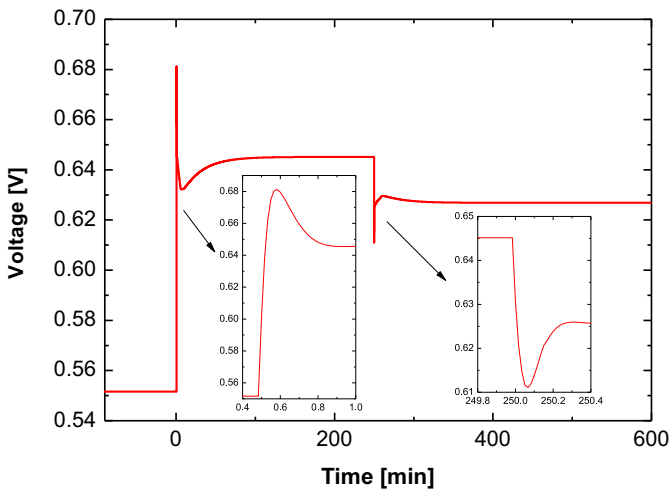


Fig. 11. Transient response of cell voltage.

under the part-load condition. As the consequent, the fuel utilization factor with the cell temperature control is also smaller than the one without any control under the constant fuel supply. The cell operating temperature doesn't dedicate an improvement of the DC efficiency sufficiently. Most effective tactic to improve the DC efficiency must be related with the appropriate fuel input corresponding to the required power output. The cell temperature control is important to prevent the performance reduction, however, the fuel utilization control should be adopted for improving the efficiency under the part-load condition.

### 3.4. Effect of functional controller terms for power output control

#### 3.4.1. Steady-state error elimination

The DC power output control with the P controller cannot eliminate steady-state error as discussed in the previous section 3.2. The steady-state error in the power output might be a problem in a certain industrial requirement. In order to solve the issue, an adoption of Proportional-Integral (PI) controller can be helpful. However, the adoption of PI controller causes longer response time until the error is sufficiently eliminated. For the solution to achieve faster response time to meet the reference value, Proportional-Integral-Derivative (PID) controller can be adequate technical option generally. The effect of the control type on the transient response of the power output is discussed.

Then the simulated SOFC operation for the power output control with adopting various controllers is shown. The time step width of the computation is set to 1[s]. The proportional gains for all controllers are set at 1 [A m<sup>-2</sup> kW<sup>-1</sup>]. The manipulated variable with the PI controller, which the integral term is added to Eq. (38), is formulated in the following equation.

$$\Delta MV = MV(t + \Delta t) - MV(t) = K_p \left[ e(t) + \frac{1}{T_i} \int_0^t e(t) dt \right] \quad (41)$$

where  $T_i$  indicates the integral time and is set at 5 [s]. The equation to describe the manipulation with PID controller, which the derivative term is added to Eq. (41), is shown as follows.

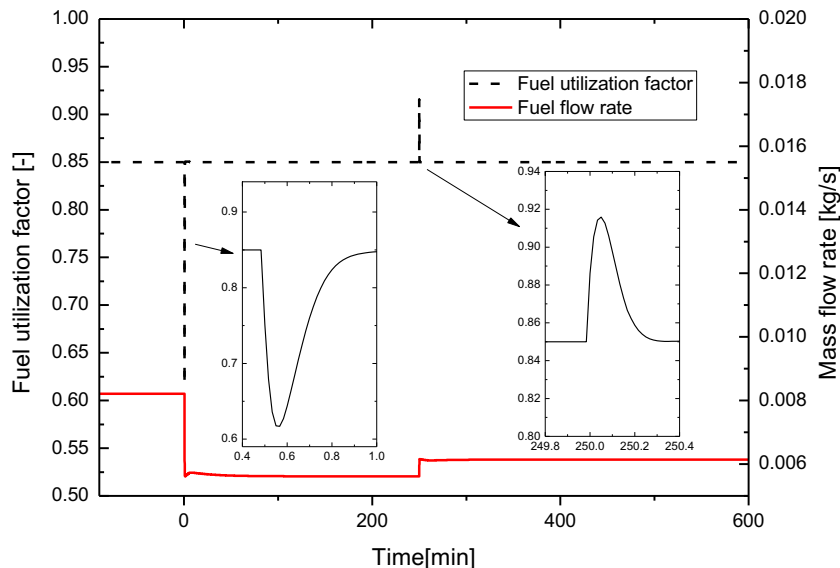


Fig. 12. Control of fuel utilization factor.

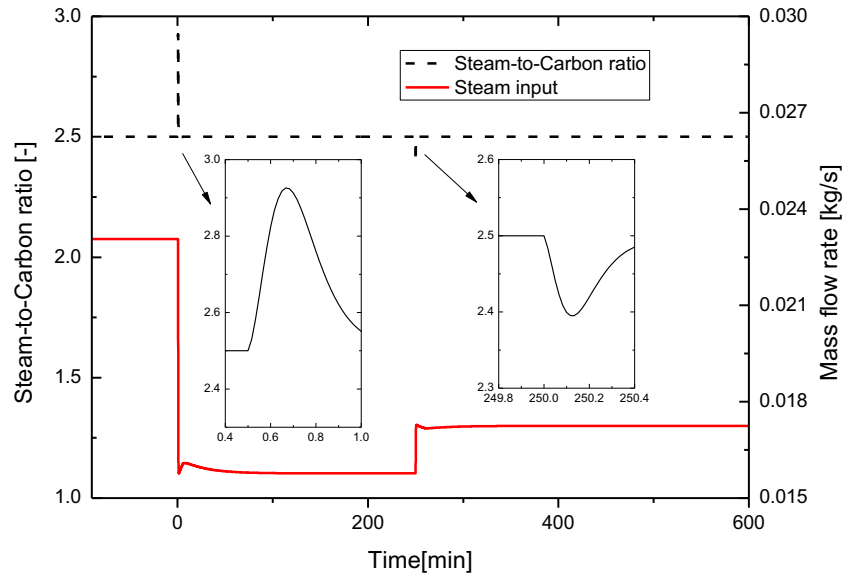


Fig. 13. Control of steam-to-carbon ratio.

$$\Delta MV = MV(t + \Delta t) - MV(t)$$

$$= K_p \left[ e(t) + \frac{1}{T_i} \int_0^t e(t) d\tau + T_d \frac{de(t)}{dt} \right] \quad (42)$$

where  $T_d$  indicates the derivative time and is set at 5 [s].

The power demand is assumed to be change from 80% to 85% at 0.5 [min]. Fig. 20 shows the DC power output responses to the load change with the P, PI and PID controllers.

Table 6 shows the relationship between the controller proportional gain and the steady-state error in the power output control with the P term. With an adoption of the P controller, the steady-state error is found about 3 [mW]. By the adjustment of the proportional gain, it is sufficiently reduced to 0.3 [mW] with the gain at 10 [A m<sup>-2</sup> kW<sup>-1</sup>]. The steady-state error can be eliminated as seen in the transient responses with the PI and PID controllers. However, the output response can easily fluctuate and demand the longer time to meet the reference, comparing to the output response obtained with P controller. The amplitude of the fluctuated response and the transient time to meet the reference can be

improved by adjusting the proportional gain and the integral time [20]. That also can be accomplished by the PID controller. But both of the response times with the PI and PID controller are longer than the one with the P controller, though the advantage of the PI and PID controllers, i.e. the residual steady-state error elimination, can be expected.

### 3.4.2. Correlation between responsiveness and fluctuation by controller specification

Elimination of the steady-state error will be appreciated. Instead of an advantage of the error elimination, the response of the power output can be fluctuated simultaneously by an effect of the controller's function. It is explicitly predicted in the previous dynamic simulation as shown in Fig. 20.

The transient response of the power output is predicted on the smaller load change from 100% to 95% and to the larger load change from 100% to 80%. Both of the predicted cases are applied with the P, PI and PID controllers and the prediction is shown in Fig. 21. It is assumed that the load change happens at time of 0.5 [min]. Fig. 21A shows the case of the controller parameter setting with  $K_p = 3$  [A m<sup>-2</sup> kW<sup>-1</sup>],  $T_i = 5$  [s],  $T_d = 5$  [s]. Fig. 21B shows the case of the

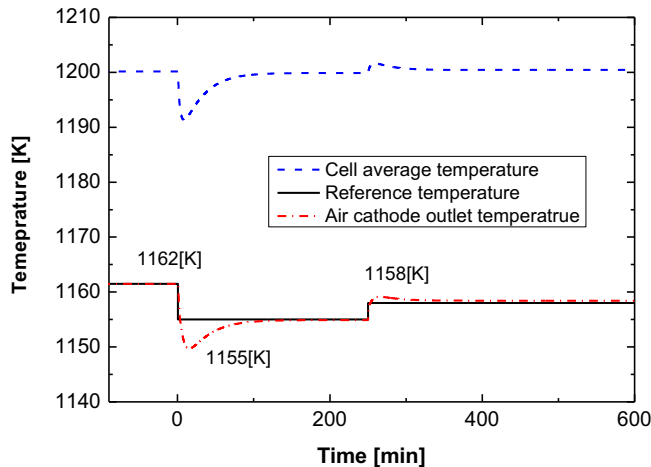


Fig. 14. Control of air cathode outlet temperature and transient response of cell average temperature.

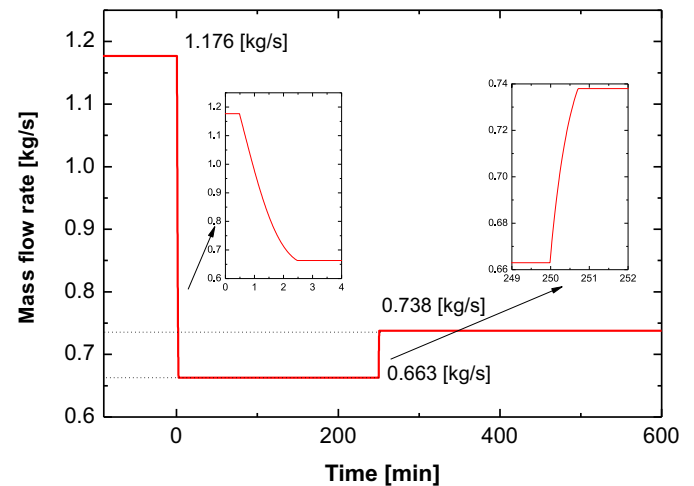


Fig. 15. Air flow rate manipulation.

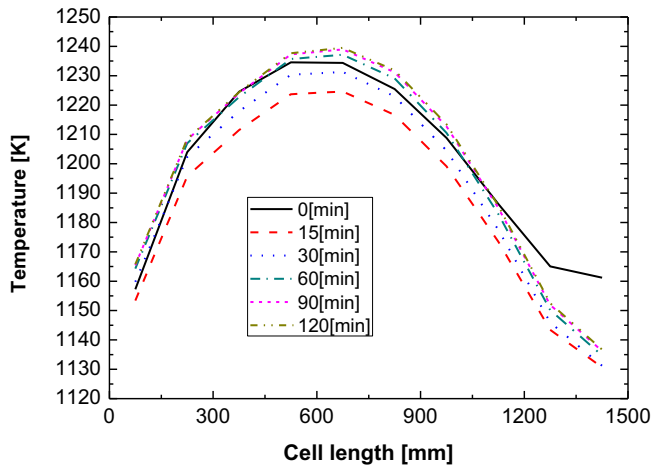


Fig. 16. Temperature distribution change of SOFC along x direction (power output from 100% to 80%).

controller parameter setting with  $K_p = 10 \text{ [A m}^{-2} \text{ kW}^{-1}]$ ,  $T_i = 1 \text{ [s]}$ ,  $T_d = 1 \text{ [s]}$ . The corrective action by the controller is assumed to be made every 1 [s]. The relatively weaker effect of the controller is observed in Fig. 21A, on the other hand Fig. 21B shows the stronger effect of the controllers' specification. It can be seen from both of the cases that the largeness of the load change magnifies the amplitude of fluctuation, where specifically the I term is added to the controller. The comparison between Fig. 21A and B shows the correlation between the responsiveness and the amplification of the predicted transient behaviors. Fig. 21A shows smaller amplitude, on the other hand Fig. 21B indicates the faster response. The complication of controller specification can be seen in the comparison. The appropriate specification must be found for the controllers, regarding the responsiveness and the amplification of the output response. Among the predicted cases, the response with the P controller is very simple and the drastic response to the load change is not predicted as it is in the cases with the PI and PID controllers. The all cases with the P controller show the very smooth response and the proportional gain corresponds to the agility of the response. Additionally, it corresponds to the quantity of remained steady-state error as previously shown in Table 6. Predicted results mentions the simplicity and the reasonability of the power output control with the P controller, if the small steady-state error is tolerated.

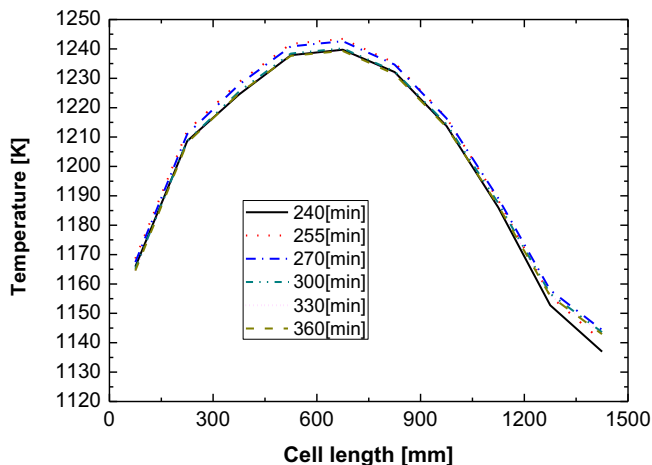


Fig. 17. Temperature distribution change of SOFC along x direction (power output from 80% to 85%).

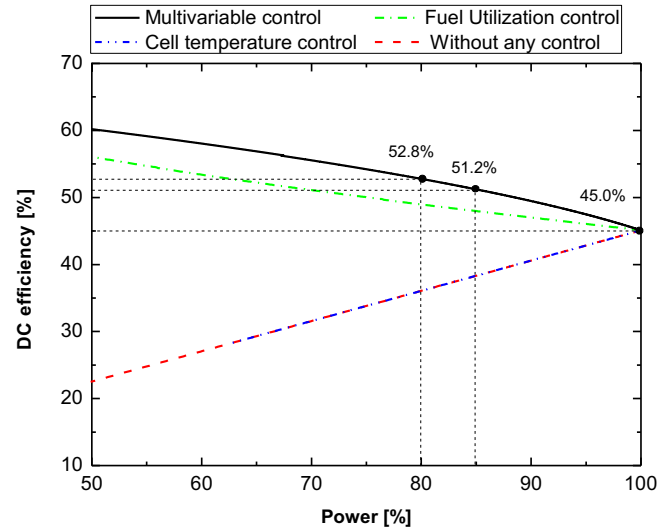


Fig. 18. DC efficiency of SOFC power generation performance under full and part-load condition. (Comparison is carried with several cases of operations with fuel utilization control, cell operating temperature control and without any control, respectively).

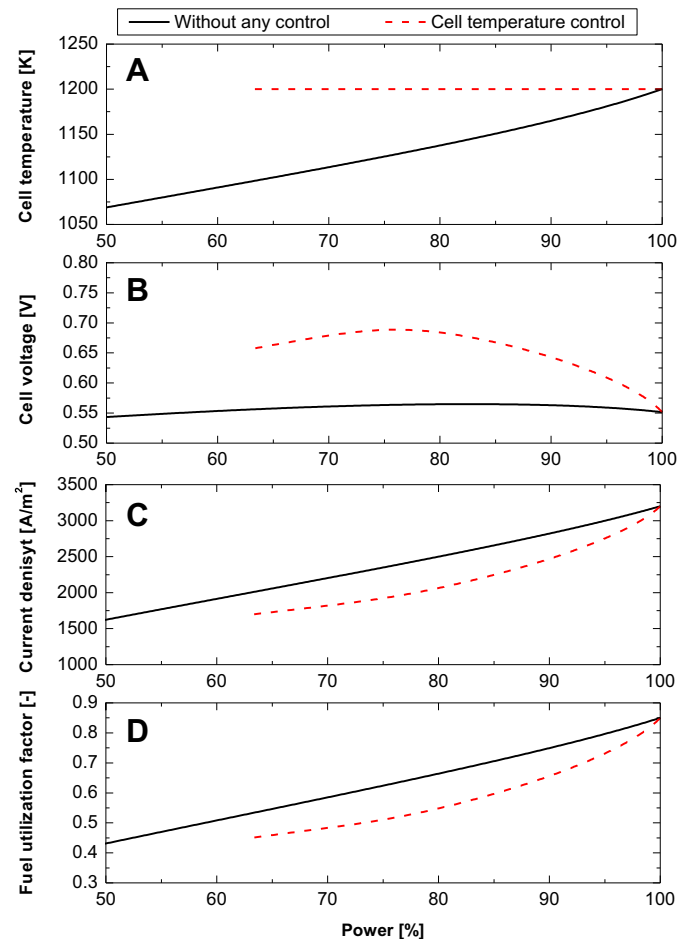
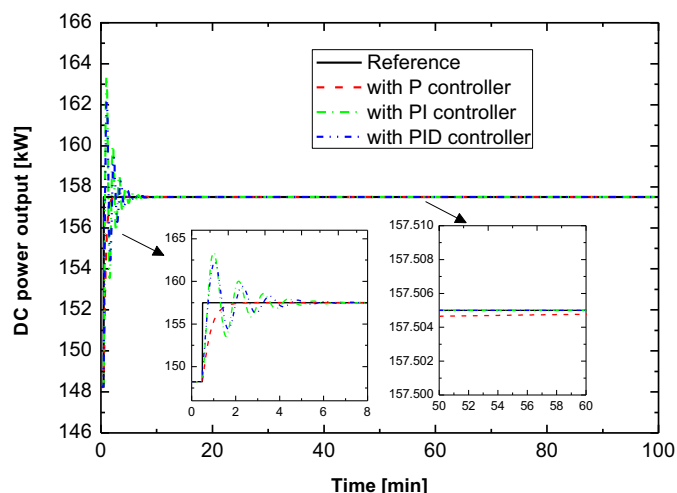


Fig. 19. Comparison of result between case with cell temperature control and case without any control. A) Cell temperature, B) cell voltage, C) current density and D) fuel utilization factor.



**Fig. 20.** Comparison between transient response of DC power outputs with P, PI and PID controllers under simulated load change from 80% to 85%, setting controller parameters at  $K_p = 1$  [ $\text{A m}^{-2} \text{ kW}^{-1}$ ],  $T_i = 5$  [s],  $T_d = 5$  [s].

### 3.4.3. Fuel starvation occurrence

Gaynor et al. have conducted numerical investigation on the prevention of the fuel starvation occurrence [33]. It was predicted that the fuel starvation can occur with the rapid load increase. For the control scheme of the power output with the current manipulation, the absolute depletion of the fuel can be caused due to the drastic current manipulation. The transient response of the DC power output is simulated to the rapid load increase from 80% to 100% with controller parameters at  $K_p = 2$  [ $\text{A m}^{-2} \text{ kW}^{-1}$ ],  $T_i = 5$  [s], and  $T_d = 1$  [s]. In the present simulation as illustrated in Fig. 22, the fuel starvation occurs at the load change where the current manipulated with the PI and PID controllers, assuming that the fuel starvation occurs where the fuel utilization factor reaches 1.0. It is noted that the presented result indicates the transient response of the fuel utilization factor just before reaching at 1.0. However, the occurrence is not predicted with the P controller adoption. As shown in Fig. 20 the responses of the DC power output with the PI and PID controllers tend to fluctuate the overshoot largely. Those behaviors in the power output can violate the fuel depletion in the power output control with the current manipulation. The transient response of DC power output is also shown in Fig. 22 with the P controller at 5 [ $\text{A m}^{-2} \text{ kW}^{-1}$ ], the fuel starvation is predicted to the load change. General control approach with the conventional controller functional terms; proportional, integral and derivative terms, it can be used in the SOFC power output control scheme. The detailed setting of the controller specification is needed to achieve the safe SOFC operation.

Furthermore, case temporary occurs while load transient where the fuel depletion violates and/or reaches close to the limitation of mass transport phenomena, precise performance analysis may be required to deliberate concentration loss. Transiently the effect of concentration polarization on the voltage response may be insignificant due to the time constant of mass diffusion phenomena in porous electrodes is very fast ( $10^{-3}$  to  $10^{-5}$  [s]) [16]. However, the effect on the steady-state performance can be matter for the SOFC which has a mechanical structure of electrode-supported [34]. Chan

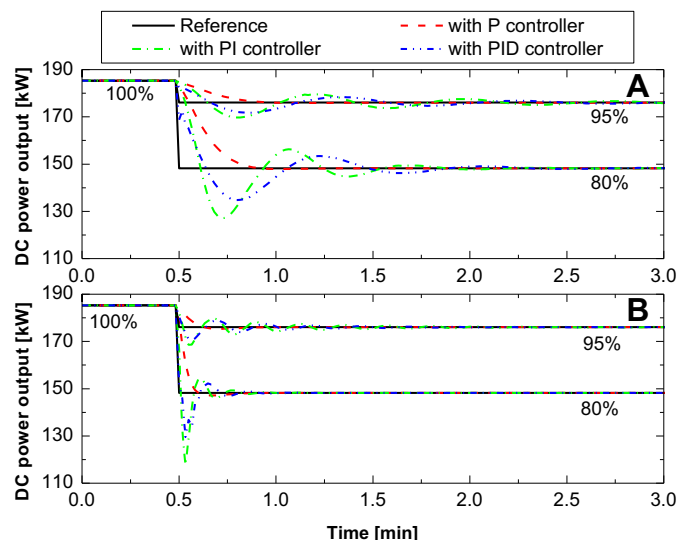


**Fig. 21.** Comparison between transient response of DC power outputs with P, PI, PID controllers under the simulated load changes from 100% to 95% and from 100% to 80%, setting the controllers parameters at A)  $K_p = 3$  [ $\text{A m}^{-2} \text{ kW}^{-1}$ ],  $T_i = 5$  [s],  $T_d = 5$  [s], B)  $K_p = 10$  [ $\text{A m}^{-2} \text{ kW}^{-1}$ ],  $T_i = 1$  [s],  $T_d = 1$  [s].

et al. have showed a precise prediction of polarization model for anode-supported, electrolyte-supported and cathode-supported SOFC structures [34]. It seems that the electrolyte-supported SOFC cannot be interfered the limitation of concentration loss comparing to the electrode-supported cells, while its thickness plays remarkable performance degradation. For electrode-supported SOFC models, the anode-supported structure is highly limited with the mass transport phenomena, perhaps due to the high fuel utilization, which can be a reference of the operation strategy as mentioned in the present study. Huang mentioned that for cathode-supported structure the performance can be limited by the high current density with the low bulk partial pressure of oxygen and its diffusivity [35]. It specifically can be matter on the cathode-supported structure at high operating temperature, since the irreversible voltage losses on this type of cell is dominated by the activation polarization [35,36]. Facing to the operation the level of control

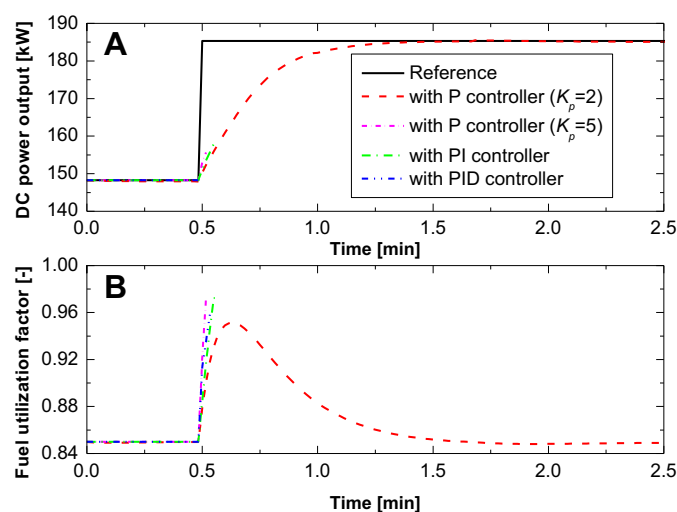


**Fig. 22.** Comparison between transient response of DC power outputs with P, PI and PID controllers under simulated load change from 80% to 100%, setting controller parameters at  $K_p = 2$  [ $\text{A m}^{-2} \text{ kW}^{-1}$ ],  $T_i = 5$  [s],  $T_d = 1$  [s]. A) DC power output, B) fuel utilization factor.

**Table 6**  
Relationship between steady-state error and proportional gain in power output control scheme.

Controller proportional gain [ $\text{A m}^{-2} \text{ kW}^{-1}$ ]	1	2	5	10
Remained steady-state error [mW]	2.8	1.5	0.6	0.3

references must be deliberated carefully to avoid such unfavorable transient cases where the operating strategy violates the physical limitation.

#### 4. Conclusions

The present paper has described transient simulation of the SOFC load-following operation with the control schemes of the cell operating temperature, the fuel utilization factor and the steam-to-carbon ratio. The procedure of the dynamic modeling was introduced and then control circuit was implemented for the all processed variables, based on the feedback control methodology. The SOFC power output, the fuel utilization factor, the S/C ratio and the air cathode outlet temperature were controlled by manipulating the current density, the fuel flow rate, the steam flow rate, and the air flow rate, respectively. The control schemes were built and the load-following operation was simulated in order to perform the highly efficient SOFC operation. Since the cell temperature measurement is very difficult, it is impossible to directly control the cell temperature. In the present study, the indirect cell temperature control by the air temperature control at the cathode outlet is proposed. The obtained results indicate efficient system operation and a control-capable response. The SOFC operation with a multi-variable control scheme may help to achieve the optimal SOFC operation. However, the cell temperature control scheme requires that both the appropriate air flow rate and air cathode outlet temperature to the power output should be set.

Effect of functional controller terms to the DC power output control scheme was also shown with the adoption of the PI and PID controllers, respectively. The result was compared to the response with the P controller adoption, and then the capability of the power output control with the P controller was shown. In the case of the load increasing operation, the fuel starvation may occur depending on the controller type and the parameter setting. The predicted results also show that a general control technic can be applied in the SOFC operation.

#### Acknowledgments

The present work was financially supported by the Polish Ministry of Science and Higher Education (Grant AGH No. 11.11.210.198) and by the Grants-in-Aid for Scientific Research of Japan (the project is referred to the number: 23561034).

#### Nomenclature

$A$	active area [ $\text{m}^2$ ]
$c$	specific heat [ $\text{kJ kg}^{-1} \text{K}^{-1}$ ]
$c_p$	specific heat of fluid under constant pressure [ $\text{kJ kg}^{-1} \text{K}^{-1}$ ]
$D$	diameter [m]
$d$	thickness [m]
$E$	activation energy [ $\text{kJ mol}^{-1}$ ]
$F$	Faraday Constant 96,485 [ $\text{C mol}^{-1}$ ] or configuration factor [–]
$\dot{G}$	Gibbs free energy change per unit time [ $\text{kJ kmol}^{-1} \text{s}^{-1}$ ]
$\bar{g}$	Gibbs free energy change [ $\text{kJ kmol}^{-1}$ ]
$h$	heat transfer coefficient [ $\text{W m}^{-2} \text{K}^{-1}$ ]
$\bar{h}_x(T)$	enthalpy of component $x$ at temperature of $T$ [ $\text{kJ kmol}^{-1} \text{K}^{-1}$ ]
$I$	current [A]
$j$	current density [ $\text{A m}^{-2}$ ]
$K$	equilibrium constant
$k$	pre-exponential factor [ $\text{mol m}^{-2} \text{bar}^{-1} \text{s}^{-1}$ ] or [ $\text{A m}^{-2}$ ]
LHV	lower heating value [ $\text{kJ kg}^{-1}$ ]

$\dot{m}$	mass flow rate [ $\text{kg s}^{-1}$ ]
$\dot{n}$	molar flow rate [ $\text{kmol s}^{-1}$ ]
$p$	pressure [kPa]
$Q$	heat source or heat transfer [ $\text{kJ s}^{-1}$ ]
$R$	universal gas constant 8.31434 [ $\text{kJ kmol}^{-1} \text{K}^{-1}$ ]
$S$	cross section area [ $\text{m}^2$ ]
$\dot{r}$	reaction rate [ $\text{kmol s}^{-1}$ ]
$r$	area specific resistance [ $\Omega \text{m}^2$ ]
$T$	temperature [K]
$t$	time [s]
$V$	volume [ $\text{m}^3$ ] or voltage [V]
$\dot{W}$	electric power [kW]
$w$	width [m]
$z$	air and fuel consumptions in molar flow rate [ $\text{kmol s}^{-1}$ ]

#### Greek letters

$\sigma$	Stefan–Boltzmann constant $5.67 \times 10^{-8} [\text{W m}^{-2} \text{K}^{-4}]$
$\eta$	power generation efficiency [%]
$\varepsilon$	electric resistance [ $\Omega \text{m}$ ] or emissivity in radiation formula [–]
$\lambda$	thermal conductivity [ $\text{W m}^{-1} \text{K}^{-1}$ ]
$\rho$	density [ $\text{kg m}^{-3}$ ]

#### Subscripts

$a$	anode
$ac$	air flow in cathode channel
$act$	activation polarization
$af$	air flow in air feed tube
$c$	cathode
$cell$	SOFC cell
$e$	electrolyte
$fa$	fuel flow in anode channel
$ff$	fuel flow in fuel feeding channel
$fp$	fuel feed plate
$fr$	fuel flow in reforming channel
$ft$	air feed tube
$i$	segment number
$j$	segment number
$int$	interconnect
$m$	average of the segment number $i$ and $i + 1$
$ohm$	ohmic polarization
$rw$	reformer wall
$0$	standard state (298.15[K], 100.00[kPa])

#### Control variable

$e(t)$	steady-state error at time of $t$ (unit depending on control scheme)
$K_p$	controller proportional gain (unit depending on control scheme)
$MV(t)$	manipulated variable at time of $t$ (unit depending on control scheme)
$T_i$	integral time [s]
$T_d$	derivative time [s]
$x(t)$	set-point of the controlled variable at time of $t$ (unit depending on control scheme)
$y(t)$	processed value at time of $t$ (unit depending on control scheme)

#### References

- [1] D. Bhattacharyya, R. Rengaswamy, Industrial & Engineering Chemistry Research (2009) 6068–6086.
- [2] J.P.P. Huijsmans, F.P.F. Van Berkel, G.M. Christie, Journal of Power Sources 71 (1998) 107–110.
- [3] P.-W. Li, K. Suzuki, Journal of The Electrochemical Society 151 (2004) A548–A557.



- [4] T. Nishino, H. Iwai, K. Suzuki, *ASME Journal of Fuel Cell Science and Technology* 3 (2006) 33–44.
- [5] A. Selimovic, M. Kemm, T. Torisson, M. Assadi, *Journal of Power Sources* 145 (2005) 463–469.
- [6] G. Brus, J.S. Szmyd, *Journal of Power Sources* 181 (2008) 8–16.
- [7] G. Brus, Y. Komatsu, S. Kimijima, J.S. Szmyd, *International Journal of Thermodynamics* 15 (2012) 43–51.
- [8] T. Nishino, J.S. Szmyd, *ASME Journal of Fuel Cell Science and Technology* 7 (2010). 051004-1–051004-8.
- [9] Y. Komatsu, S. Kimijima, J.S. Szmyd, *ECS Transactions* 25 (2009) 1061–1070.
- [10] C. Stiller, B. Thorud, S. Seljebø, Ø. Mathisen, H. Karoliussen, O. Bolland, *Journal of Power Sources* 141 (2005) 227–240.
- [11] H. Uechi, S. Kimijima, N. Kasagi, *ASME Journal of Engineering for Gas Turbines and Power* 126 (2004) 755–762.
- [12] P. Costamagna, L. Magistri, A.F. Massardo, *Journal of Power Sources* 96 (2001) 352–368.
- [13] S. Campanari, *ASME Journal of Engineering for Gas Turbines and Power* 122 (2000) 239–246.
- [14] Y. Komatsu, S. Kimijima, J.S. Szmyd, *Energy* 35 (2010) 982–988.
- [15] D. Bhattacharyya, R. Rengaswamy, C. Finnerty, *Chemical Engineering Science* 64 (2009) 2158–2172.
- [16] R.S. Gemmen, C.D. Johnson, *Journal of Power Sources* 144 (2005) 152–164.
- [17] F. Mueller, F. Jabbari, R. Gaynor, J. Brouwer, *Journal of Power Sources* 172 (2007) 308–323.
- [18] C. Stiller, B. Thorud, O. Bolland, R. Kandepu, L. Imsland, *Journal of Power Sources* 158 (2006) 303–315.
- [19] Y. Zhu, K. Tomsovic, *Electric Power Systems Research* 62 (2002) 1–11.
- [20] Y. Komatsu, S. Kimijima, in: *Fuel Cells Science and Technology 2010*, Elsevier B.V., Zaragoza, 2010.
- [21] T.W. Song, J.L. Sohn, J.H. Kim, T.S. Kim, S.T. Ro, K. Suzuki, *Journal of Power Sources* 142 (2005) 30–42.
- [22] R.A. George, *Journal of Power Sources* 86 (2000) 134–139.
- [23] J. Wei, E. Iglesia, *Journal of Catalysis* 224 (2004) 370–383.
- [24] E. Achenbach, *Journal of Power Sources* 49 (1994) 333–348.
- [25] E. Achenbach, E. Riensche, *Journal of Power Sources* 52 (1994) 283–288.
- [26] N.F. Bessette II, W.J. Wepfer, J. Winnick, *Journal of The Electrochemical Society* 142 (1995) 3792–3800.
- [27] N.F. Bessette II, W.J. Wepfer, *Journal of Energy Resources Technology* 117 (1995) 43.
- [28] K. Tanaka, C. Wen, K. Yamada, *Fuel* 79 (2000) 1493–1507.
- [29] F.P. Incropera, D.P. DeWitt, *Fundamentals of Heat and Mass Transfer*, sixth ed., John Wiley & Sons, Inc., 2006.
- [30] M. Fardadi, F. Mueller, F. Jabbari, *Journal of Power Sources* 195 (2010) 4222–4233.
- [31] Y. Inui, N. Ito, T. Nakajima, A. Urata, *Energy Conversion and Management* 47 (2006) 2319–2328.
- [32] F. Mueller, F. Jabbari, J. Brouwer, *Journal of Power Sources* 187 (2009) 452–460.
- [33] R. Gaynor, F. Mueller, F. Jabbari, J. Brouwer, *Journal of Power Sources* 180 (2008) 330–342.
- [34] S.H. Chan, K.A. Khor, Z.T. Xia, *Journal of Power Sources* 93 (2001) 130–140.
- [35] K. Huang, A. Zampieri, M. Ise, *Journal of The Electrochemical Society* 157 (2010) B1471–B1478.
- [36] X. Li, N. Xu, X. Zhao, K. Huang, *Journal of Power Sources* 199 (2012) 132–137.